Multi-variable rotor dynamics optimization of an aerostatic spindle

Author(s):
Stoop, Fabian; Meier, Severin; Civelli, Patrick; Mayr, Josef; Wegener, Konrad

Publication date:
2023-06

Permanent link:
https://doi.org/10.3929/ethz-b-000596730

Originally published in:
CIRP Journal of Manufacturing Science and Technology 42, https://doi.org/10.1016/j.cirpj.2023.01.006

CIRP Journal of Manufacturing Science and Technology 42 (2023) 12–23

Contents lists available at ScienceDirect

CIRP Journal of Manufacturing Science and Technology

journal homepage: www.elsevier.com/locate/cirpj

Multi-variable rotor dynamics optimization of an aerostatic spindle

Fabian Stoop [a,*], Severin Meier [a], Patrick Civelli [a], Josef Mayr [b], Konrad Wegener [a]

[a] Institute of Machine Tools and Manufacturing (IWF), ETH Zürich, Zürich, Switzerland
[b] inspire AG, Zürich, Switzerland

ARTICLE INFO

Available online xxxx

Keywords:
Rotor dynamics
Machine tool
Spindle
Aerostatic spindle
Single-objective multi-variable optimization

ABSTRACT

Single-objective multi-variable rotor dynamics optimization promotes the design of spindles in sustainable production. The goal is efficient partial automation of the design process and the optimization of the spindle shaft. The Timoshenko-Ehrenfest beam theory together with the Latin hypercube sampling and direct optimization methods are selected principles. The parametric model and frequency analysis, as well as the transient analysis, are key resources for rapid system development. Challenges are the computational effort to find the steady state of the milling simulation for the optimization problem. In addition, this entire process must meet overall performance requirements during the system design phase. The outlined concept is based on rotor dynamics optimization and validated for an aerostatic spindle in a milling process. The validation measurements are performed according to ISO 230-7 on the aerostatic spindle.

Introduction

Microsystem technology is one of the largest growing markets in the world. This branch of the industry places high demands on the production of components and thus also on the development of the machine tools used for this purpose. A core piece of such a machine tool is the spindle, which houses the spindle rotor shaft. A multi-variable optimization of a classical machine tool roller-bearing spindle is described by Tong et al. [1]. During the operation of an air-bearing spindle, complex dynamic effects occur for this rotor as described by Dupont [2], which represents a challenge during the planning phase. Multi-variable optimization of grooved gas journal bearings itself is investigated by Guenat et al. [3] for robustness in manufacturing tolerances. Due to the high complexity, there is a risk that aspects of the rotor behavior are only discovered late in the development phase. As described by Ehrlenspiel et al. [4], this can cause high costs and set back the system design of the machine development process. If, on the other hand, everything is taken into account right from the start, there is a risk of getting lost in details that do not advance the project at this early stage. The integrated design and optimization of the whole direct-drive turbomachinery with a gas-bearing supported rotor is elaborated by Schiffmann et al. [5]. It is important to be able to make estimates of the system behavior without much effort, thus giving the development team the freedom to concentrate on conceptual tasks before dealing in detail with the system in the detailed system design. To support the design process, a novel method for partial automation of the simulation of the rotor behavior in operation is therefore developed within the scope of the present work. Cao et al. [6] introduced a virtual simulation method of milling operations to model the spindle behavior. Furthermore, a suggestion for a suitable geometry of the rotor should be able to be derived depending on framework conditions such as nominal speed, installation space, bearing characteristics, etc. This combination of a steady-state milling simulation together with a multi-variable rotor optimization is shown for the first time in this work.

State of the art

Various approaches exist for the design of rotors. The methods considered in this paper deal with the analytical formulation as well as the discretized formulation. A rough overview of the analytical methods for the analysis of a rotor is given by Genta [7]. The flexible behavior of rotors was treated in detail in a publication by Jeffcot [8]. Therefore, the simplest mathematical formulation of a rotor is often referred to as a Jeffcott rotor. Here, a massless shaft with a point mass is studied, which can be considered for different boundary conditions. In the simplest case, the rotor is a rigidly mounted rotor. However, the bearings can also have a stiffness while the shaft is assumed to be rigid, or both approaches can be combined. Since no moments of inertia are taken into account in the Jeffcot model, the mathematical formulation is comparatively simple. However, it is also not possible to carry out any analyses that depend on them, which can strongly influence the dynamic behavior of the rotor. To

* Corresponding author.
E-mail address: stoop@iwf.mavt.ethz.ch (F. Stoop).

https://doi.org/10.1016/j.cirpj.2023.01.006

take the moments of inertia into account in the analysis, the Jeffcot model is extended for three cases. Either a flexible shaft with a disc mass or a rigid shaft with arbitrary axisymmetric geometry is considered. All these analytical formulations of a rotor only allow an approximate description of the effective behavior. Therefore they are only conditionally suitable both for analysis and for a design proposal. To be able to describe the rotor realistically, the finite element method (FEM) is therefore normally used today. In the best case, analytical methods can only be used for a rough estimation.

The volume elements normally used in commercial software, such as tetrahedra or cuboids, make it possible to represent the material behavior very realistically. According to Steinke [9], the basic idea of the FEM is to divide complex geometries into a finite number of elements that are easy to calculate and which, when considered together, give a very good approximation of the behavior of the complex geometry. However, these element types are not well suited for the present case of a rotor with a focus on computational performance. Therefore, beam elements should be used for the discretisation of the rotor.

Beam theory

Beam elements are characterized by their simplicity, wherefore they are better suited than volume elements concerning the required computing power. Beam elements have only two nodes, one at each end of the element. For the mathematical description of the real behavior of a beam, simplifying assumptions are normally made. Two simplifying theories exist for the description of beams, the Euler-Bernoulli beam theory (EBB) and the Timoshenko-Ehrenfest beam theory (TEB). The EBB assumes that there are no shear stresses and shear deformation in the system. It is therefore a shear-rigid formulation of the beam. As shown in Fig. 1, when the beam is bent, the free cross-sectional area of the beam remains constant, undeformed and perpendicular to the neutral axis. Since a realistic consideration of the warping of the free surface involves a considerable mathematical effort, a simplifying assumption is made for the TEB. A more physically correct description does also include the warping of the surface, which is implemented for Timoshenko elements, by Poganski et al. [10]. The shear stress τ_{xz} and shear strain γ_{xz} are assumed to be the average shear stress τ_m and shear strain γ_m over the beam cross-section. These averaged values are constant across the cross-section of the beam and result in an angular change and distortion of the free surface but the cross-sectional area is flat and not perpendicular to the neutral axis. This is shown in Fig. 1b). For the formulation of the TEB, the assumptions of bending without considering shearing as in the EBB and that of the averaged shear stress τ_m and strain γ_m are now superimposed, which is shown in Fig. 1c). The change in shear area compared to the cross-sectional area is taken into account in the TEB using the shear correction factor κ. This shear correction factor was implemented according to Hutchinson [11].

$$\kappa = \frac{6(r_i^2 + r_o^2)^2(1+\nu)^2}{7r_i^4 + 34r_i^2r_o^2 + 7r_o^4 + \nu(12r_i^4 + 48r_i^2r_o^2 + 12r_o^4) + \nu^2(4r_i^4 + 16r_i^2r_o^2 + 4r_o^4)} \quad (1)$$

Where r_o and r_i are the outer and inner radius of the annular cross-section and Poisson's ratio ν of the material used. This formulation is only valid for thick-walled cross-sections. It gives more accurate results than the widely used formulation according to Cowper [12], as shown by Hutchinson [11].

This shows that EBB is a special case of TEB. Comparing EBB and TEB, it is easy to see that EBB is a good approximation of the material behavior for long, slender beams where the effects of bending play a much larger role than those of shear and sliding. In contrast, TEB can be used for arbitrary ratios of the length and cross-section of a beam and still approximates the beam behavior correctly. For this reason, the TEB is more suitable for the formulation of the rotor, which for example requires a very short beam element with a large diameter for the thrust bearing.

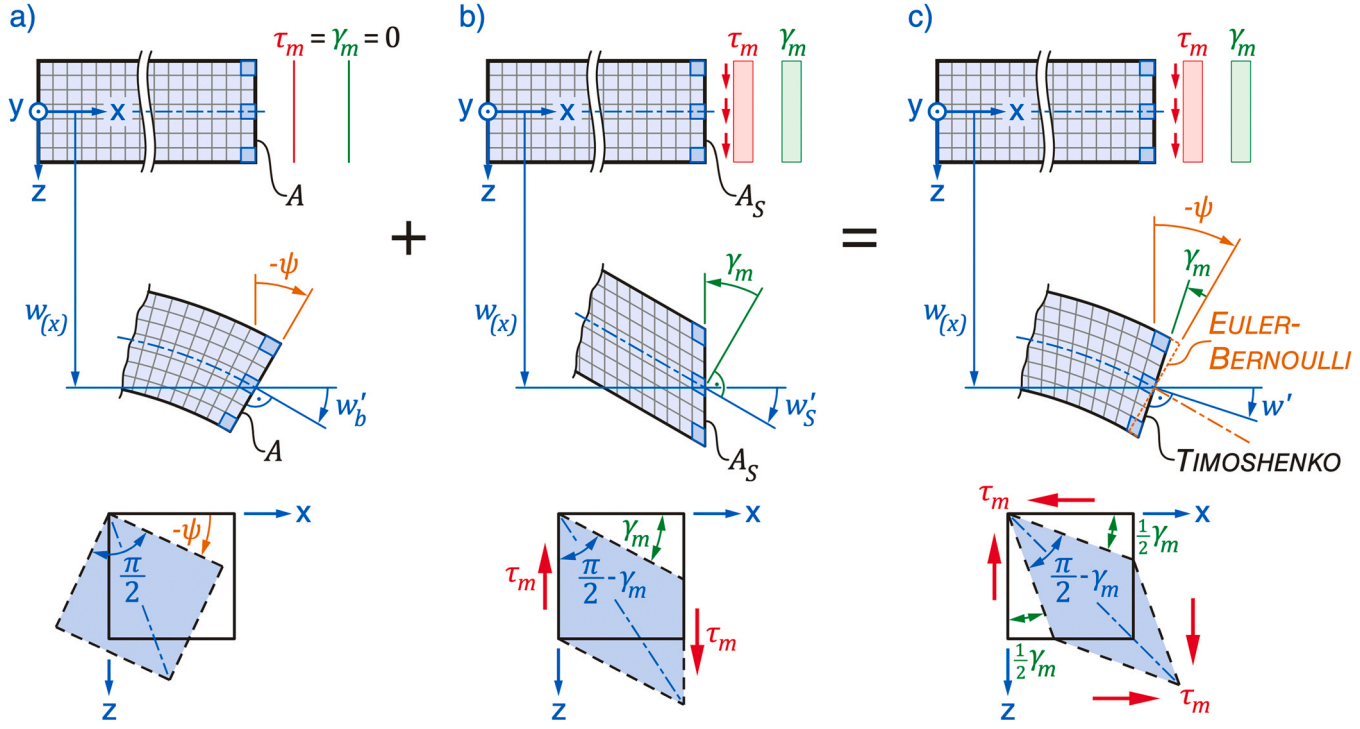

Fig. 1. Illustration of beam models a) Euler-Bernoulli beam theory with bending but without shear. b) A beam without bending with averaged shear stress and shear strain. c) Combination of EBB and the assumption of averaged shear results in the Timoshenko-Ehrenfest beam theory illustrated by Spura [13].

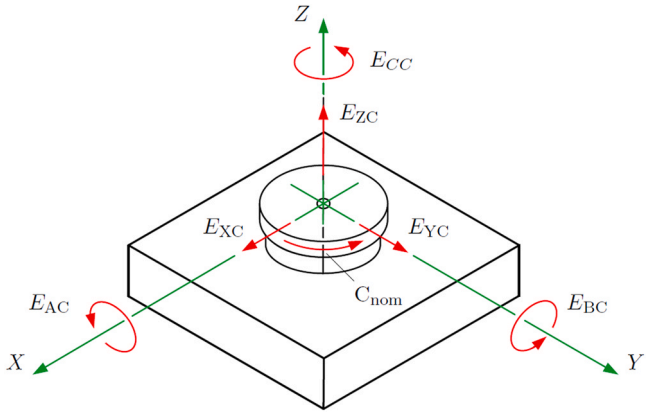

Fig. 2. Error motion according to ISO 230-7:2015 [14].

Spindle error model

Rotary axes, such as spindles, can have positioning and motion errors. Positioning errors are orientation errors of the axis itself concerning the machine coordinate system. According to ISO 230-7, there are five errors (A0C, B0C, Y0C, X0C, C0C) if the axis is a purely rotary axis, C0C can be ignored. Additionally, there are multiple error motions possible during the turning of an axis, which can be seen in Fig. 2. These are of special importance, as such movements influence the surface quality directly as well as the precision of the workpiece. However, unless the rotational position of the spindle is important, error movement ECC can be ignored.

Another important distinction is made between synchronous and asynchronous error motions, whereby the first correlates with the rotation of the spindle, while the latter does not. The asynchronous error motion is calculated concerning the rotation center of the machine polar chart center (PC), whereas for the synchronous error, a circle approximation is needed, and the error is then calculated concerning the calculated center point. These are usually calculated by using the Gauss approximation least-squares center (LSC). The difference between the two can be seen in Fig. 3.

Method

The optimized spindle shaft is achieved through the beam element formulation combined with the frequency and transient analysis input in the multivariable optimization. The following section elaborates on these required principles in depth.

Element formulation of the rotor shaft

The shape functions of the element are implemented according to Luo [15]. In comparison to the traditional formulation, the one described by Neto et al. [16], has the advantage of being free of the so-called shear locking effect. The shear locking effect describes an artificial, numerical stiffening of the elements, which can lead to incorrect solutions. For the derivation of the shape functions, an element is considered in the deformed and undeformed state as shown in Fig. 4.

The derivation according to Luo [15] yields to the homogeneous Euler-Lagrange equations which are simplified for symmetric cross-sections.

$$EA\frac{\partial^2}{\partial x^2}u_{C,x} = 0 \tag{2}$$

$$\kappa GA\left(\frac{\partial^2}{\partial x^2}u_{C,y} - \frac{\partial}{\partial x}\theta_z\right) = 0 \tag{3}$$

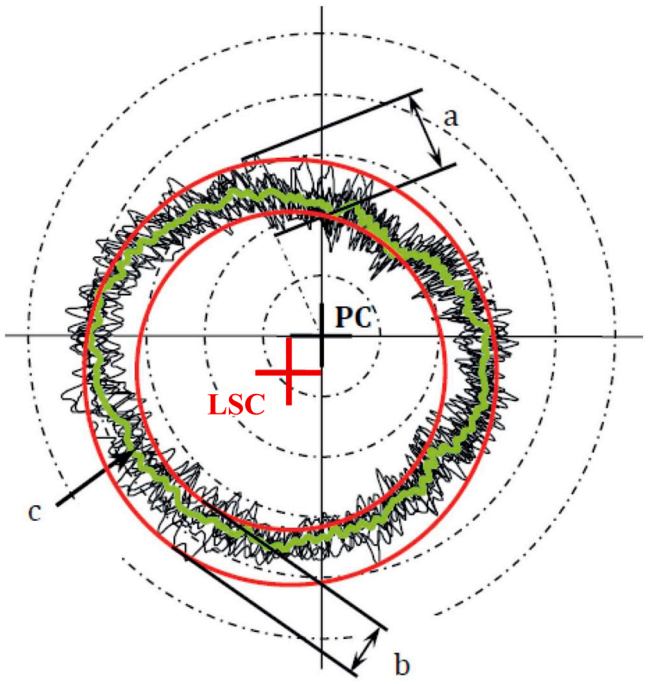

Fig. 3. Synchronous and asynchronous error motion with a) asynchronous error motion value based on PC center, b) synchronous error motion value based on LSC center, c) synchronous error motion plot according to ISO 230-7:2015 [14].

$$\kappa GA\left(\frac{\partial^2}{\partial x^2}u_{C,z} + \frac{\partial}{\partial x}\theta_y\right) = 0 \tag{4}$$

$$\kappa G(I_y + I_z)\frac{\partial^2}{\partial x^2}\theta_x = 0 \tag{5}$$

$$EI_y\frac{\partial^2}{\partial x^2}\theta_y + \kappa GA\left(\frac{\partial}{\partial x}u_{C,z} + \theta_y\right) = 0 \tag{6}$$

$$EI_z\frac{\partial^2}{\partial x^2}\theta_z - \kappa GA\left(\frac{\partial}{\partial x}u_{C,y} - \theta_z\right) = 0 \tag{7}$$

With the nodal deformation u, θ according to Fig. 4, E the elastic modulus, A the cross-sectional area, G the shear modulus, I the moment of inertia. Inserting the boundary conditions at the two nodes N_{e1} and N_{e2} and solving for the six degrees of freedom ultimately yields the field functions of the beam element given by:

$$u_{C,x}(x) = N_1 u_{C,x,1} + N_2 u_{C,x,2} \tag{8}$$

$$u_{C,y}(x) = H_{u_{C,y1}} u_{C,y1} + H_{\theta_{z,1}}\theta_{z,1} + H_{u_{C,y2}} u_{C,y2} + H_{\theta_{z,2}}\theta_{z,2} \tag{9}$$

$$u_{C,z}(x) = H_{u_{C,z,1}} u_{C,z1} + H_{\theta_{y,1}}\theta_{y,1} + H_{u_{C,z,2}} u_{C,z,2} + H_{\theta_{y,2}}\theta_{y,2} \tag{10}$$

$$\theta_x(x) = N_1\theta_{x,1} + N_2\theta_{x,2} \tag{11}$$

$$\theta_y(x) = G_{u_{C,z,1}} u_{C,z,1} + G_{\theta_{y,1}}\theta_{y,1} + G_{u_{C,z,2}} u_{C,z,2} + G_{\theta_{y,2}}\theta_{y,2} \tag{12}$$

$$\theta_z(x) = G_{u_{C,y1}} u_{C,y1} + G_{\theta_{z,1}}\theta_{z,1} + G_{u_{C,y2}} u_{C,y2} + G_{\theta_{z,2}}\theta_{z,2} \tag{13}$$

The element shape functions N, H and G are now extracted from the field functions and the beam element is fully describable by the nodal deformations alone.

Equation of motion

The equation of motion for FEM can be derived in different ways. Either via Hamilton's principle, described by Neto et al. [16], or with the help of Galerkin's method as shown by Klein [17]. Here, the equation of motion is used with the help of the Lagrange equation of

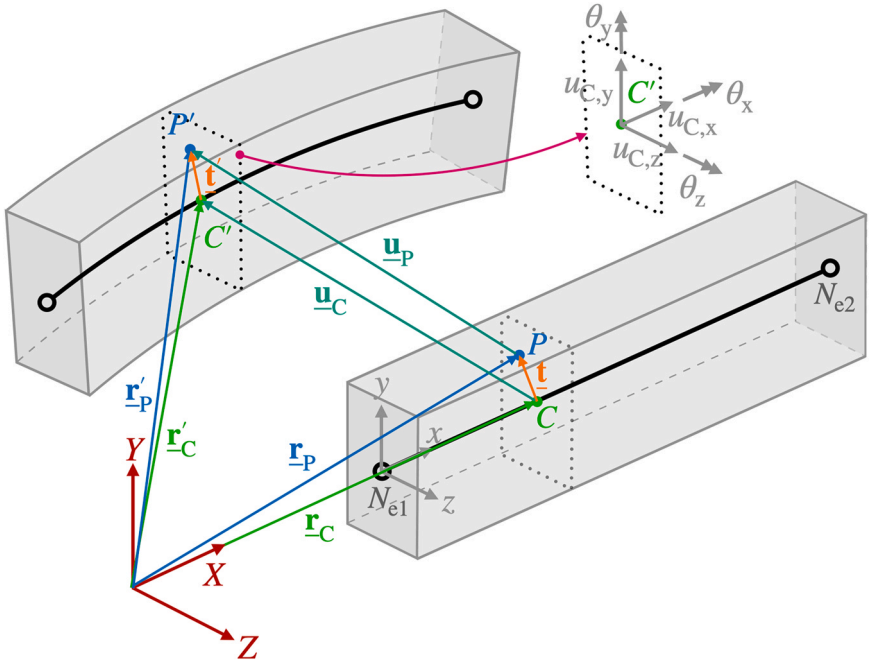

Fig. 4. Beam element in the deformed and undeformed state with the chosen coordinate system.

the second-order according to Vollan et al. [18]. Two formulations with their respective advantages and disadvantages can be used to represent the equation of motion of a rotor. These formulations refer either to a reference system that rotates with the rotor or to a stationary reference system. For which cases the respective descriptions are applicable is described by Kumar [19]. Since the bearing properties can be direction-dependent and the rotor is symmetrical, the system in this work is formulated in a space-fixed reference frame. The equation of motion thus takes the following form, based on the general equation (15):

$$\underline{\underline{M}}_g\ddot{\underline{q}} + (\underline{\underline{C}}_{M,g} + \underline{\underline{C}}_{B,g} + \underline{\underline{G}}_g)\dot{\underline{q}} + (\underline{\underline{K}}_{E,g} + \underline{\underline{K}}_{B,g} + \underline{\underline{K}}_{C,g})\underline{q} = \underline{f}_{b,g} + \underline{f}_{s,g} + \underline{f}_{p,g} \tag{14}$$

With M_g the global mass matrix of the system, q the degrees of freedom of the beam element, C_M the material damping matrix, C_B the bearing damping matrix, G_g the gyroscopic matrix, K_E the element stiffness matrix, K_B the bearing stiffness matrix, K_C the circulatory matrix, f_b the body load, f_s the surface load and f_p the point load. Nelson et al. [20] describe the advantage of a rotating frame system that is used for isotropic systems with symmetric bearing stiffness and damping. The order of the system matrices is smaller compared to fixed frame formulation and therefore requires less computing effort.

Frequency analysis

The aim of the spindle rotor frequency analysis is to identify the critical excitation frequencies of the system. An excitation frequency is considered critical if it coincides with the resonance/natural frequency of the system. The natural frequencies of the rotor itself are derived from solving the 'free-free problem'. However, the natural frequencies calculated there only apply to the rotor without boundary conditions. To find the natural frequencies of the system under consideration of the bearings, an extended eigenvalue problem must be formulated for the frequency analysis. For this purpose, the formulation according to Larsonneur [21] is used. The equation of motion in its general form is:

$$\underline{\underline{M}}\ddot{\underline{q}} + \underline{\underline{C}}\dot{\underline{q}} + \underline{\underline{K}}\underline{q} = \underline{f} \tag{15}$$

This is a second order differential equation that cannot be used to find the natural frequencies directly. To do so, it must first be transformed into the state-space form. According to Shaw et al. [22], this ultimately leads to the complex conjugate eigenvector ϕ_I which corresponds to the first order, state-space formulation. This eigenvector can then be split in two which allows for the extraction of the second order eigenvectors ϕ_{II} and $\lambda\phi_{II}$ where each has the same number of entries as the original second-order system had equations.

$$\underline{z} = \begin{pmatrix} \underline{q} \\ \dot{\underline{q}} \end{pmatrix} = \underline{\Phi}_I e^{\lambda t} = \begin{pmatrix} \underline{\Phi}_{II} \\ \lambda\underline{\Phi}_{II} \end{pmatrix} e^{\lambda t} \tag{16}$$

Furthermore, it is seen from this that the first half of the eigenvector corresponds to the displacements of the respective degrees of freedom, while the second half corresponds to the velocities. If one now considers the complex conjugate eigenvectors of the displacements ϕ_{II}, the direction of the orbital motion is determined according to Pedersen [23]. The absolute deformation of the rotor axis is first calculated with:

$$u = Nq \tag{17}$$

Where u is the complex deformation along the neutral axis, N is the matrix of shape functions and q is the complex eigenvector of nodal displacements ϕ_{II}. Then the cross product of the imaginary part of u with the real part of u is formed.

$$\underline{w} = \mathrm{Im}(\underline{u}) \times \mathrm{Re}(\underline{u}) \tag{18}$$

The direction of w indicates the direction of the orbital motion of the shaft. If w points in a positive direction along the rotation speed vector, it is called a forward whirl, in the case that w points in the opposite direction, it is called a backward whirl.

Transient analysis

Various methods have been developed for the transient analysis of mechanical systems. For the transient analysis, the Generalized-α-Method (CH-α) has been used according to Chung et al. [24]. It is relatively simple in its implementation and offers the advantage that it can map various precursor methods like Newmark-β through

suitable parameter selection. To describe the CH-α method, the modified equation of motion is considered:

$$\underline{\underline{M}}\underline{a}_{n+1-\alpha_m} + \underline{\underline{C}}\underline{v}_{n+1-\alpha_f} + \underline{\underline{K}}\underline{d}_{n+1-\alpha_f} = \underline{f}\,(t_{n+1-\alpha_f}) \tag{19}$$

With the two algorithmic parameters:

$$\alpha_m = \frac{2\rho_\infty - 1}{\rho_\infty + 1},\ \alpha_f = \frac{\rho_\infty}{\rho_\infty + 1} \tag{20}$$

Where ρ_∞ describes the degree of numerical dissipation at high frequencies.

Rotor optimization

The optimization, or rather the generation of a design proposal, builds on what was discussed before and brings together the components that have been worked out so far. In this section, the boundary conditions for the optimization problem are first defined and a brief overview of the procedure is given. Afterwards in the implementation, the individual steps that finally lead to the design proposal are discussed in detail.

A large number of different optimization algorithms exist, each better or worse suited for a particular problem. It is therefore necessary to select a suitable procedure for optimizing the rotor. According to Stryk et al. [25], optimization procedures can be divided into two main groups:

Direct: These procedures require a mathematical description of the problem, the so-called objective function. Based on this, an optimum is then found using, for example, gradient-based methods. Starting from a fixed starting point, a direct method will always find the same optimum. Whether this optimum is global or local depends on the objective function and the starting position.

Indirect: These methods can also be used with a large number of measurements. The problem can therefore be both mathematically defined as an objective function or a large number of measurements. Indirect methods are not based on mathematical approaches like direct methods but find their way to an optimum through clever trial and error. This requires a large number of evaluations of the problem. In contrast to the direct methods, indirect methods cannot guarantee finding the same optimum, although, the starting positions are fixed.

The displacement at the end node of the tool is selected here as the so-called target variable. This should be kept as small as possible during operation. This displacement is the result of the geometry-dependent, transient analysis of the system. For the calculation of the cutting forces, the model according to Altintas et al. [26] was implemented. The underlying idea is that the cutting edge does not leave a smooth surface in the workpiece. However, to perform the optimization, a fixed value for the tooltip displacement is needed, which will never be possible with Altintas' model. Therefore, the model is only used to find an average value of the steady-state. With this average value, the response surface fitting can be carried out. It is therefore not a mathematical description of the objective function. This, therefore, rules out the application of direct optimization methods. Indirect methods could theoretically be applied. However, due to the large number of evaluations required for the problem under consideration, indirect methods are also not applicable, as they simply require too much computing power and time. A possible solution to carry out a time-efficient optimization is to formulate a mathematical objective function that describes the system behavior approximatively. The optimization variables chosen for the problem are shown in Fig. 5.

For the optimization variables shown in Fig. 5, ranges of permissible values are defined as the lower and upper limits. The limits chosen for the rotor shaft under consideration are listed in Table 1.

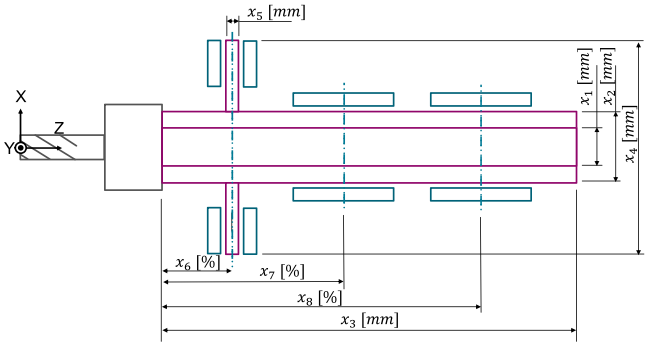

Fig. 5. Optimization variables for the calculation of a geometry proposal of the rotor shaft. The thrust and journal air bearings are illustrated in blue boxes and the shaft geometry is in purple.

The values have to be between these limits. The simplest way to do this is to select the values randomly. However, this involves the risk of unwanted correlations between the optimization variables, which can falsify the result. A better choice for sampling is the Latin Hypercube Sampling (LHS) method. Here, quasi-random values are defined for each optimization variable within its bounds. To select these points, it is first necessary to determine how many values are to be generated. In contrast to random selection, the LHS, as described by Zio [27], requires a smaller number of values to make statistical estimates. Furthermore, the LHS method can minimize the correlations between the values. A disadvantage of the LHS method is, that the list of generated values cannot be extended, as is the case with randomly generated values.

Implementation and setup

The implementation describes the calculation process from the modeling of the rotor shaft and sensitivity analysis to the final optimization. Furthermore, the actual measurement setup to validate the simulation and optimization results are also discussed and described.

Sensitivity analysis

After the geometries of the r shaft have been generated using the LHS method as described in the previous section, a transient analysis is performed for each of these geometries. The steady-state displacements $d_{i,end}$ at the end node of the tool together with the respective geometry information are stored. For the calculation of the cutting forces, the model according to Altintas [28] was implemented:

$$F_a(\phi) = K_{ac} b h(\phi) + K_{ae} b \tag{21}$$

$$\mathrm{F}_r(\phi) = K_{rc} b h(\phi) + \mathrm{K}_{re}\mathrm{b} \tag{22}$$

$$F_t(\phi) = K_{tc} b h(\phi) + K_{te} b \tag{23}$$

With K_{ac}, K_{rc} and K_{tc} the coefficients of internal forces, K_{ae}, K_{re} and K_{te} the coefficients of frictional forces, depth of cut b and the dynamic chip thickness $h(\phi)$. This model takes into account the regenerative effect (chatter) during the end milling process. The underlying principle is that the cutting edge does not leave a smooth surface in the workpiece. For the application and tool considered here, however, only a speed of 10'000 rpm is relevant. Therefore, the spindle is evaluated and optimized for a tool with 3 cutting edges and a diameter of 8 mm. Of course, this can also be extended to the analysis for different speeds, but this would then result in a significantly larger parameter space. The corresponding model parameters are listed in Table 2:

Table 1
Lower and upper limits of the selected optimization variables for the rotor shaft.

Optimization variable	Lower limit	Upper limit	Unit	Description
x_1	3	10	mm	Inner diameter rotor shaft
x_2	20	40	mm	Outer diameter rotor shaft
x_3	200	300	mm	Length of rotor shaft
x_4	50	70	mm	Outside diameter of thrust bearing
x_5	4	8	mm	Thickness of thrust bearing
x_6	0.05	0.2	-	Position of the axial bearing
x_7	0.2	0.4	-	Position of the front radial bearing
x_8	0.5	0.8	-	Position of the rear radial bearing

Table 2
Transient cutting force model parameter.

Spindle speed	10′000 rpm
Number of cutting edges	3
Cutting edge angle	45°
Feed velocity	25′000 mm/min
Tool diameter	8 mm
Axial depth of cut	0.5 mm
K_{ac}	-100 MPa
K_{ae}	10 N/mm
K_{rc}	236 MPa
K_{re}	20 N/mm
K_{tc}	800 MPa
K_{te}	19 N/mm

The representation of the end milling process at selected points in time during the simulation is shown in Fig. 6. The simulation starts at t = 0. The material to be machined (thick black line) is directly in front of the tool. For t = 1.4 ms to t = 8.6 ms it can be seen how the tool penetrates further into the material. From t = 10.1 ms onwards the tool is in full engagement. The process forces, both radial and tangential, as well as the forces along the main are shown as arrows.

From these results, correlations between the optimization variables and the resulting displacements are found. The Pearson correlation coefficient is used for this. The correlations between all variables are determined and as the result, a correlation matrix P is found. The values contained in P lie in the range $-1 \leq p_{ij} \leq 1$. Such a correlation matrix is shown in Fig. 7. The components on the matrix diagonal always have the value 1, since the correlation of a variable with itself always corresponds to 1.

The matrix is also symmetrical meaning either the last row or column represents the correlations between the optimization variables and the target variable. The various aspects of the sensitivity analysis can be read very quickly. The correlations within the optimization variables should be as small as possible, which is indicated by small dots in Fig. 7. If these correlations are too large, the correlations to the target variable may be distorted. In the last column or row, the large dots indicate a strong correlation between the respective optimization variable and the target variable. The correlations found are dependent on the number of geometries generated. The correlations among the optimization variables become smaller as the number of samples increases. The relevant correlations of the target variable with the optimization variables become clearer as the number of samples increases. The number of samples for this analysis is set to 50. This number was experimentally evaluated for the range between 10 and 200 and the best tradeoff between convergence and computational efficiency was found in 50 samples.

Modeling of the rotor shaft and optimization

The first design proposal is generated based on the sensitivity analysis. As illustrated in Fig. 8, the beam element representation is simplified compared to the detailed rotor geometry. The implemented test mandrel with a length of 121 mm and an average diameter of 16 mm and tool holder with a length of 63 mm and an average diameter of 28 mm represents the largest permitted tool, which therefore brings the greatest dynamics to the shaft. The manufacturing tolerances and the connection points of different elements and materials are assumed as ideal. Furthermore, the whole geometry is made mainly out of steel. The few little other materials like magnets for the rotor are neglected.

The bearing positions are illustrated in Fig. 8 with red marks. The stiffness and damping characteristics of the bearings are derived as described in Stoop [29]. These values are mainly dependent on the speed and eccentricity during operation. However, these operating conditions are derived from the use case and assumed to be static for this analysis of the rotor dynamics over the excitation range. Furthermore, the stiffness and damping of air bearings are also dependent on the diameter of the bearing. However, this dependency can be considered in the design of the air bearings for the corresponding diameters and the bearings can thus also be designed for different diameters with the same stiffness and damping. Furthermore, the two radial bearings are symmetrically designed and thus have the same characteristics. The appropriate values for the main speed of 10′000 rpm are given in Table 3.

The mathematical model, meta-model, which is used for optimization, is created with the help of linear regression. In doing so, an attempt is made to match a polynomial of degree g with m independent variables, a so-called response surface approximation (RSA), as closely as possible to the point cloud of results $d_{i,end}$ found through the transient analysis. The determination of the RSA is done according to the procedure described by Arora [30]. The quality of the RSA found compared to the determined data points of the system response is quantified with the help of the coefficient of determination R^2. The closer R^2 is to 1, the better the RSA represents the system behavior. If $R^2 = 0$, the RSA only represents the mean value of the data points.

Spindle measurement setup

The spindle error analyzer (SEA) by Lion Precision uses a precise double master ball target with a roundness error of less than 50 nm as a reference and five capacitive sensors to capture the movements of the target mounted to the spindle. Four of the capacitive sensors point in the radial direction (P1, P4, P2, P5) and one additional along the spindle axis (P3). The sensors are placed as shown in Fig. 9, in line with the corresponding X, Y and Z axis of a rectangular system. Therefore, component errors such as tilt movements around the X and Y axis are measured (i.e. EAC, EBC), as well as deviations in X, Y and Z directions (EXC, EYC, EZC). However, location errors (A0C, B0C) cannot be detected. Additionally, the SEA distinguishes between synchronous and asynchronous errors. Moreover, simultaneous temperature measurement of a maximum of 7 different sensors is possible and synchronized with the displacement measurements.

Accordingly, the following tests are possible to be performed according to ISO 230-7 standards: radial rotating sensitive direction, radial fixed sensitive direction, tilt fixed sensitive direction, axial error motion, thermal stability and temperature variation error.

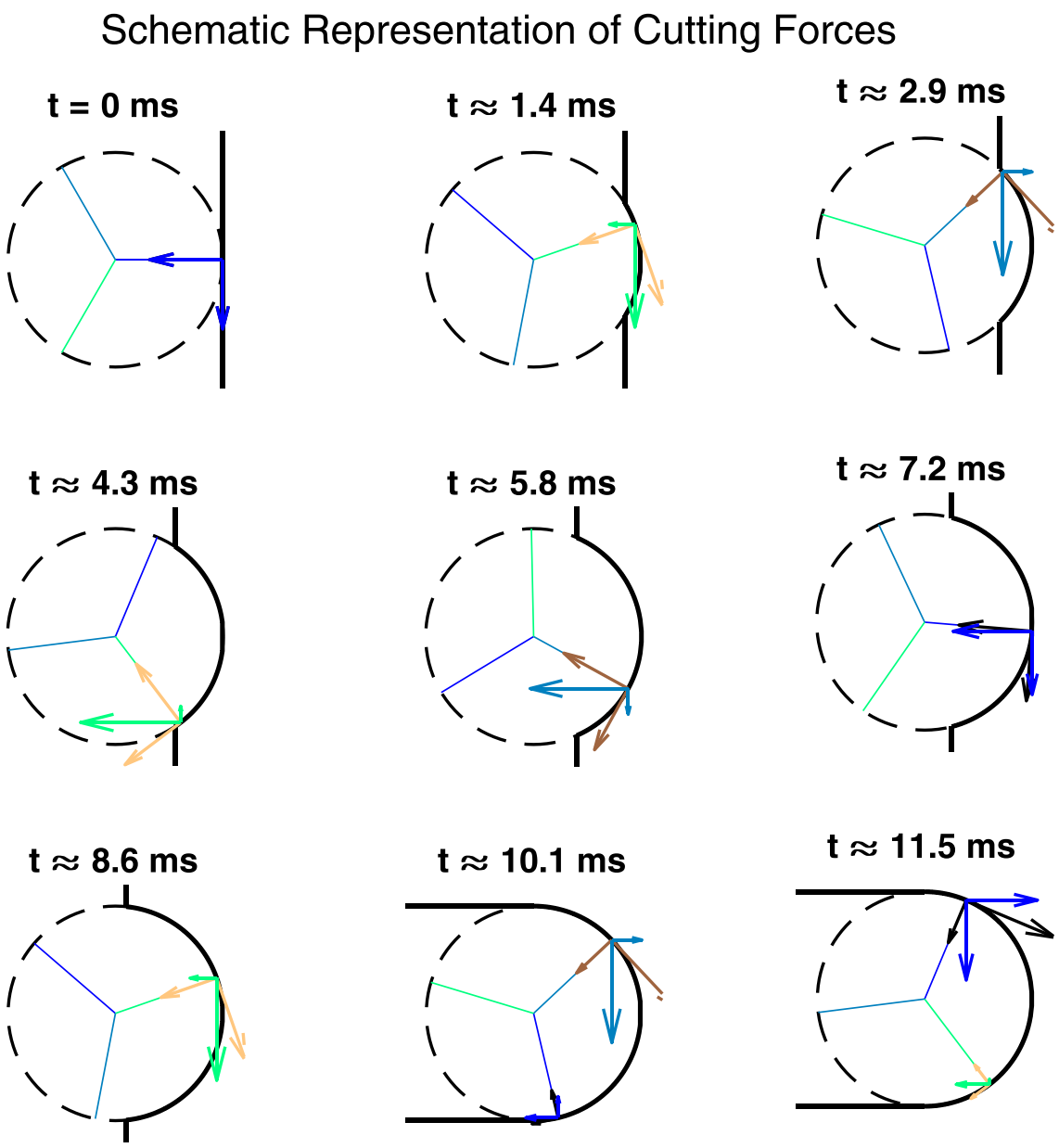

Fig. 6. Transient material penetration of the end milling process.

Axial error motions are categorized into fundamental, residual synchronous, and asynchronous motions. Fundamental error motions occur at the rotational frequency of the spindle, whereas residual motions occur every integer multiple of a rotation. Asynchronous axial error motions on the other hand do not repeat regularly with the rotation of the spindle. Fixed sensitive direction measurements set the sensitive direction when the workpiece is rotated and the point of measurement is not rotating. Such a measurement represents best the situation in a turning process. All variation in this direction results in 1:1 errors on the workpiece, whereas motions in tangential direction only reflect on the workpiece as deviations of second-order magnitude.

Contrary thereto, rotating sensitive direction measurements are of importance for drilling or milling operations. Therefore, movements in both directions must be considered when calculating deviation. The radius at any given angle is calculated as mentioned in ISO 230-7 [14]:

$$r(\theta) = r_0 + \Delta X(\theta)\cos(\theta) + \Delta Y(\theta)\sin(\theta) \quad (24)$$

With θ being the angle of rotation, $\Delta X(\theta)$ the output of the displacement sensor in the x-direction, $\Delta Y(\theta)$ the output of the displacement sensor in the y-direction and r_0 the value to scale the plot.

Results

The results of the geometry optimization are shown in Fig. 10. In this paper, the RSA is performed using two of the eight independent variables as can be seen in Fig. 10. However, any number and combination of independent variables can be used, shifting the problem into higher dimensions. The two variable cases shown here have been chosen for illustrative purposes. These are the outer diameter of the rotor shaft and the outer diameter of the thrust bearing disc. These two values together form the main description of the rotor outer diameter geometry. The target parameter in the form of the tooltip displacement is also shown in the figure. Here, 100 geometries have been calculated for the problem. The RSA of order 12 found has a coefficient of determination R^2 of 0.97, which is a good approximation of the behavior.

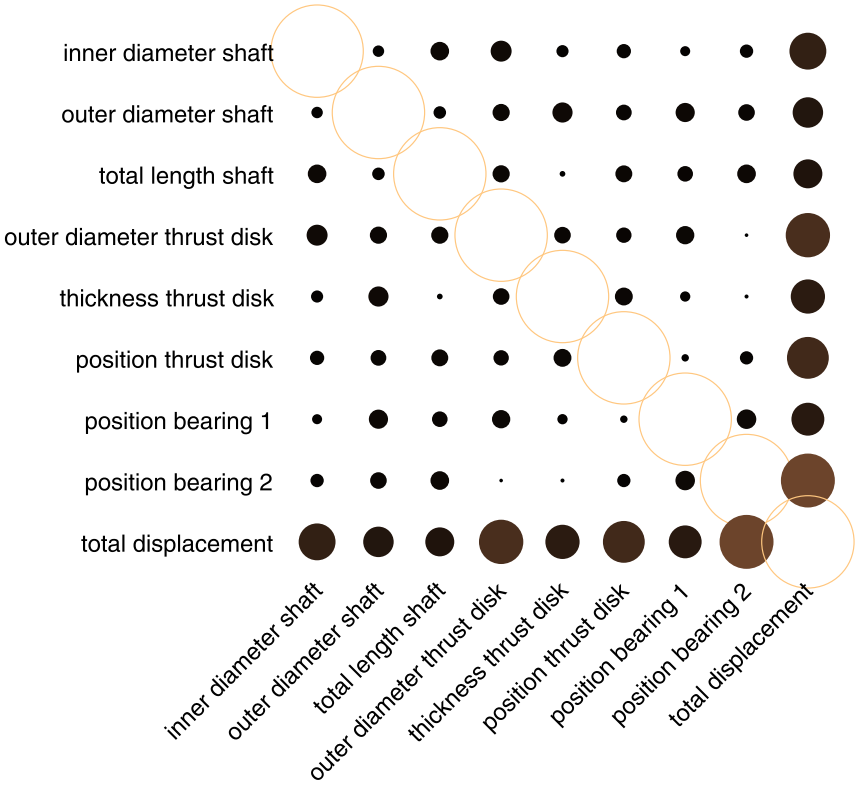

Fig. 7. Sensitivity matrix on the main design parameters and the total displacement.

The blue circle in Fig. 10 shows the optimum of the two design parameters. The final parameter selection is shown in Table 4. However, these are only the parameters of the spindle shaft itself. The description of the tool and tool holder is implemented for the largest permitted tool and holder.

Table 3
Gas bearing properties at 10′000 rpm.

	Stiffness	Damping
xx-direction	18.4 N/µm	1025 Ns/m
yy-direction	18.3 N/µm	611 Ns/m

Frequency and transient analysis

For the geometry found through the optimization process, a frequency analysis is now performed. The resonance frequencies found are typically shown in the so-called Campbell diagram as in Fig. 11. The influence of the rotational speed is seen in the bending modes. For isotropic radial bearings, for example with identical properties in both coordinate directions of the bearing cross-section, the resonance frequencies coincide at $\Omega = 0$. These bearing properties can be assumed for a standing spindle rotor where gravity acts in the axial direction of the rotor. For increasing speeds $\Omega > 0$, the frequency splits into two lines drifting apart. The lower resonance frequency corresponds to a backward whirl, and the higher one to a forward whirl. If the excitation frequencies coincide with the resonance frequencies, marked in green, the associated speed corresponds to the critical speed.

The stability of the system is seen from the sign of the damping coefficient σ, which is the real part of the eigenvalue. Further typical diagrams for the analysis of a damped rotor are the root locus

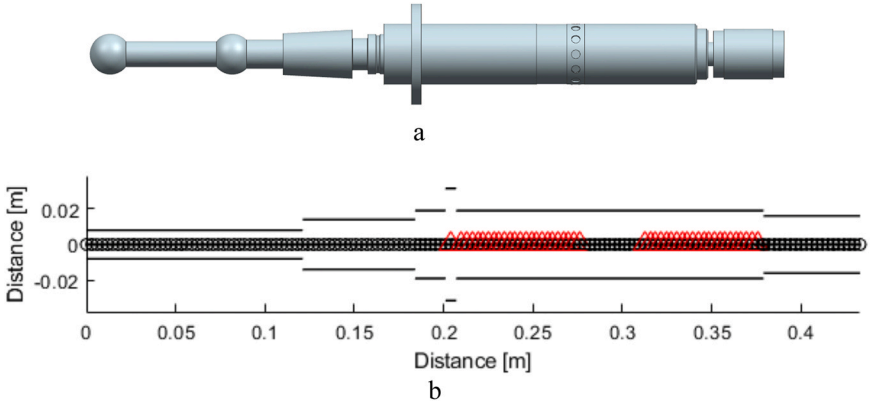

Fig. 8. The rotor geometry with all details is at the top and the nodal beam element representation is shown below. The beam elements of 3 mm length are shown in black and the additional bearing conditions are in red.

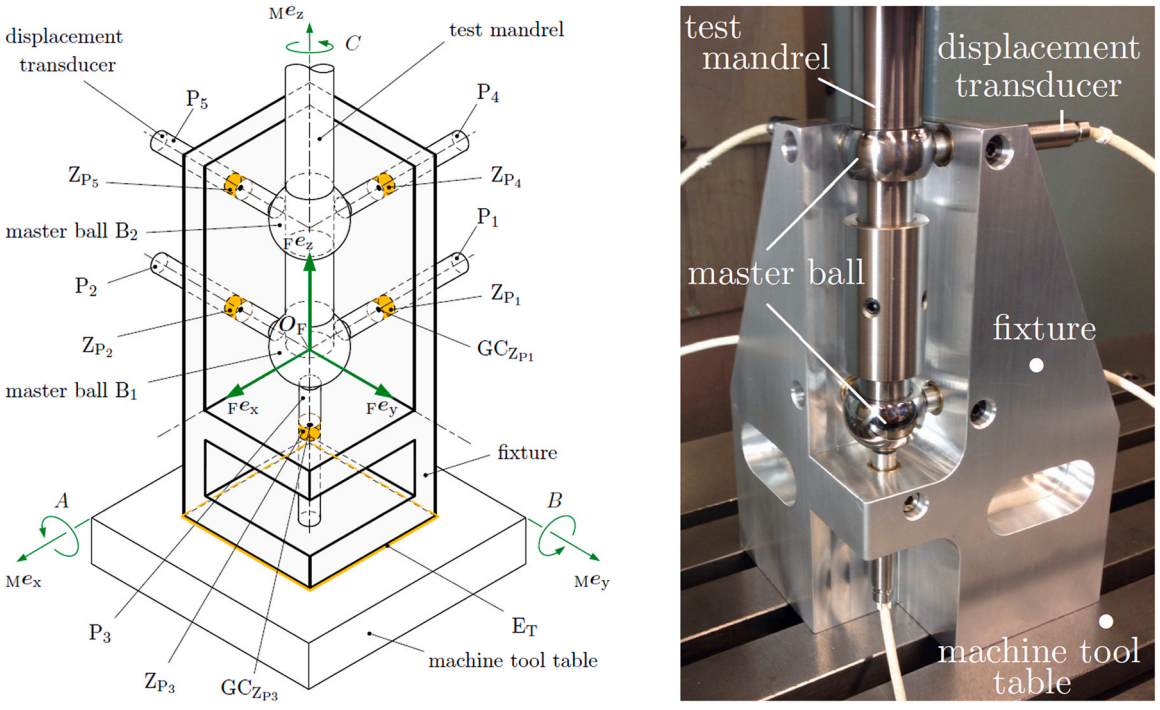

Fig. 9. ISO fixture according to Böhl [31].

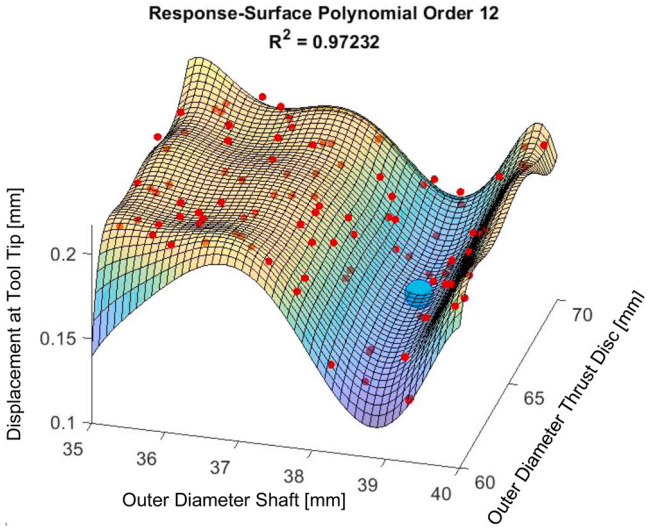

Fig. 10. Response-Surface Approximation of the target and two design parameters. The red dots represent the calculated values and the blue circle is the corresponding optimum.

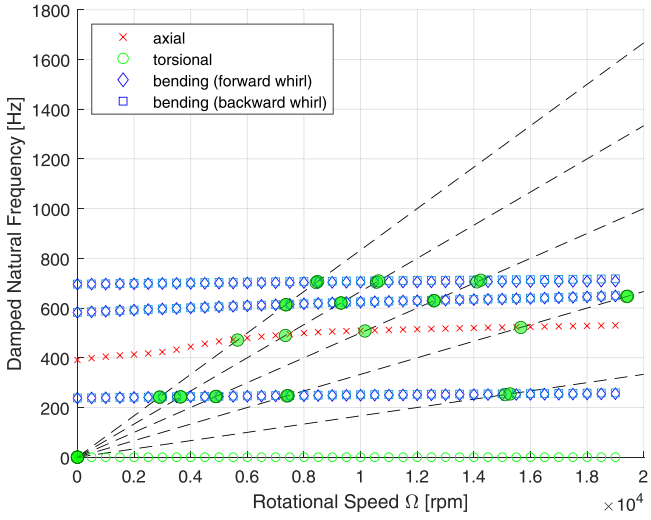

Fig. 11. Campbell diagram for the important natural frequencies with the corresponding rotational speed.

Table 4
The resulting design parameters.

Parameter	Result	Unit	Description
x_1	5	mm	Inner diameter rotor shaft
x_2	38	mm	Outer diameter rotor shaft
x_3	250	mm	Length of rotor shaft
x_4	63	mm	Outside diameter of thrust bearing
x_5	6	mm	Thickness of thrust bearing
x_6	0.08	-	Position of the axial bearing
x_7	0.24	-	Position of the front radial bearing
x_8	0.64	-	Position of the rear radial bearing

diagram as shown in Fig. 12 and the simulated radial rotating sensitive synchronous error in Fig. 13 out of the transient analysis. In Fig. 12, it is seen at a glance whether the system becomes unstable at any time. The vertical axis describes the imaginary part of the eigenvalues which are also known as the damped frequency. In the diagrams shown here, this is never the case over the entire speed range. This can be seen from the fact that the green circles, namely the torsional modes, come very close to the value zero and are therefore considered borderline stable. The eigenvalues move with increasing speed towards the positive direction of the decay rate this behavior can be explained by the gyroscopic effect on the rotor. Since the bearing stiffness is described as constant, it is estimated that the natural frequency is only affected by the shaft rotor dynamics. The

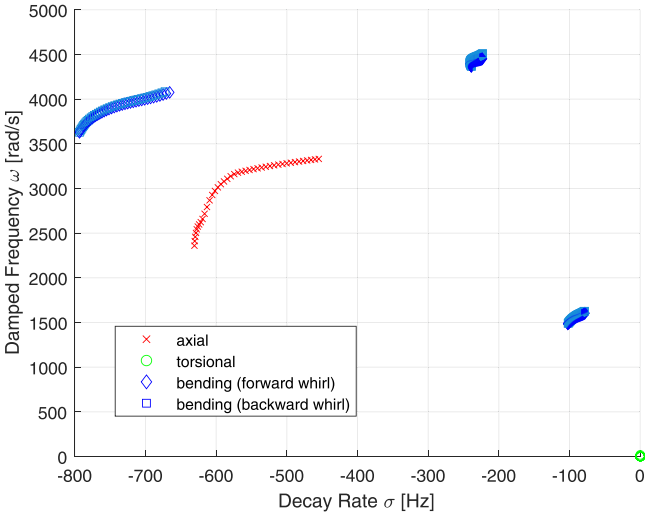

Fig. 12. Root locus diagram of the real part and imaginary part of the eigenvalues.

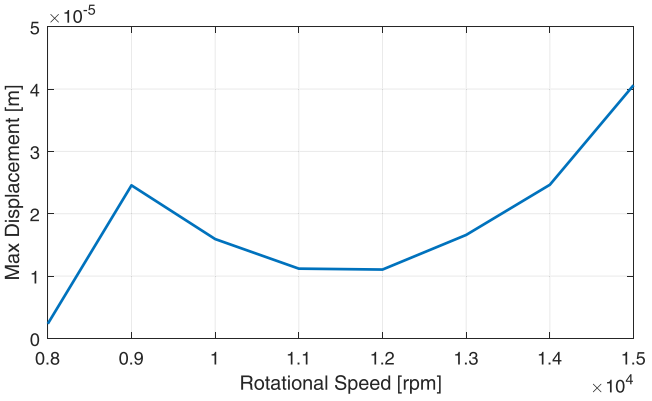

Fig. 13. Simulated radial rotating sensitive synchronous error.

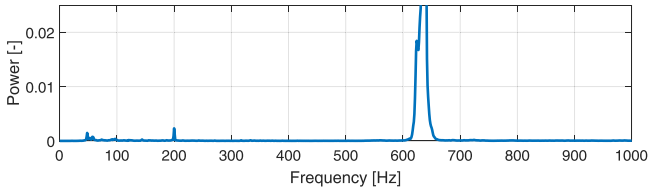

Fig. 14. Measured mean tooltip frequency response function at 0 rpm.

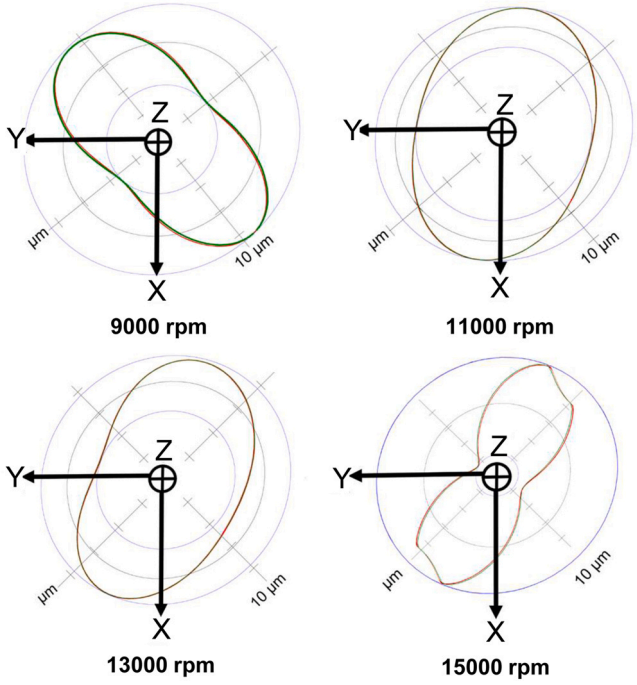

Fig. 15. Measured radial rotating sensitive polar plots.

fact that primarily the torsional modes are almost borderline stable is explained by the fact that this represents the only degree of freedom of the system, that is not supported by the bearings.

The simulated radial rotating sensitive synchronous error in Fig. 13 is calculated with the implemented rotor dynamic model and the residual mean unbalance excitation of 4.5 gmm for the whole rotor. This excitation and the eigenmodes then represent the illustrated errors.

Frequency response function

For the first verification of the developed model, the Frequency Response Function (FRF) of the rotor is measured. This measurement is elaborated according to the method using the sound emission spectrum analysis presented by Akbari et al. [32]. This allows quick and comparatively simple measurement of the natural frequencies. In the present case, of course, the measurement is carried out with the test mandrel, tool holder and spindle shaft in the assembled state. The frequencies can then be compared according to the Campbell diagram in Fig. 11. The results of this impact test are shown in Fig. 14. No statement can be made about the power, as only the sound emission is recorded. The test is again carried out several times to minimize the noise of the individual recordings. The results up to a frequency of 1 kHz show an agreement of the natural frequencies in the range of approx. 200 Hz and approx. 600–700 Hz with the calculated Campbell diagram. Furthermore, a natural frequency at approx. 50 Hz can be seen in Fig. 14, which is probably due to an unsuppressed rigid-body movement during the measurement.

Error movement measurement

The optimized rotor geometry is analyzed according to the described test setup. The corresponding errors, in terms of synchronous and asynchronous errors to the ideal behavior, are shown in Fig. 15. The amplitude of the deflection and the corresponding phase is shown. The position angle of the ellipse changes depending on the speed. Furthermore, the greater semi-axis of the orbits is also partly dependent on the speed. The measured radial error at 15′000 rpm shows two harmonics. Whereby the superimposed harmonic is affected by the 3rd harmonic of the rotation as seen in the Campbell diagram. The main stimulus of this effect may also come from a superimposed imbalance of the rotor.

In addition, the rotating sensitive synchronous error amplitudes are shown in Fig. 16. Here, the natural frequency is known from the frequency analysis in form of bending at approx. 9′000 rpm is visible in the form of an amplitude increase in this range. The further increase in amplitude towards 15'000 rpm comes from the increasing influence of the unbalance and a first eigenmode over 20′000 rpm. This residual static and dynamic unbalance due to manufacturing tolerances are included in the rotor dynamics model. The unbalance is included using a first and second-order excitation of the

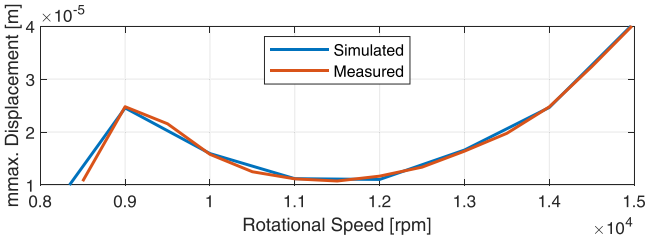

Fig. 16. Measured and simulated radial rotating sensitive synchronous error.

eccentricity in the mass of the rotor. It is neither the part tolerance nor the assembly errors directly but the resulting eccentricity of the center of mass in the rotational direction. Further, the asymmetry of the bearing itself and the bearing position can influence this excitation. Furthermore, the measured results in Fig. 16 match the simulated values from Fig. 13 well. The remaining root-mean-square error (RMSE) is 0.28 µm between the simulation and the measurement. Whereas the Euler-Lagrange equations from (2) to (7) and the corresponding shear correction factor from Eq. (1).

This proposed spindle shaft thus shows a well-describable behavior in terms of minimum displacement at the tool center point. Furthermore, the described frequency and transient analysis take only a few seconds per speed level and design point. In addition, the dynamic behavior is already in good agreement with the experimental results and therefore provides valuable insights without a physical experiment.

Conclusion and outlook

The basic procedure for an initial design proposal of an aerostatic spindle using FEM and optimization is shown. The dynamic characteristics are formulated and implemented using beam theory and afterwards used together with the frequency and time transient cutting force analysis.

Numerous extensions to the current implementation are possible. If it is assumed, that the bearings will always have isotropic properties, meaning the system is not subjected to non-uniform volume forces related to the axes of the radial bearings, then the system can be formulated in body-fixed coordinates. A good derivation of such a formulation is described by Kirchgässner [33]. This formulation will open up the possibility of representing a rotor with non-symmetrical cross-sections if cooling fluid is to be conducted through the rotor. In this case, of course, the shape functions of the Timoshenko elements would have to be recalculated with the complete system of Euler-Lagrange equations.

For the present analysis, manufacturing tolerances were also neglected. If, for example, the center of mass deviates from the theoretical neutral axis, centripetal forces arise, which can negatively influence the behavior of the rotor. For the formulation of the Timoshenko elements, it was assumed that the cross-sectional can distort relative to the neutral axis, but it is always assumed to be flat. A more physically correct description would also include the warping of the surface.

The combination of the presented steady-state milling simulation together with the multi-variable rotor optimization is elaborated in this paper. Furthermore, extensions are easily possible based on the described model due to the computational efficiency of the whole procedure. This means that the adoption of completely different applications is possible, such as the design of turbo compressors, high-speed rotor systems or other applications that combine precision and speed.

Declaration of Competing Interest

The authors declare that they have no known competing financial interests or personal relationships that could have appeared to influence the work reported in this paper.

Acknowledgements

The authors would like to thank the Swiss Innovation Agency - Innosuisse for the financial support during the project.

References

[1] Tong, V.C., Hwang, J., Shim, J., Oh, J.S., Hong, S.W., 2020, Multi-objective Optimization of Machine Tool Spindle-Bearing System. International Journal of Precision Engineering and Manufacturing, 21:1885–1902. https://doi.org/10.1007/s12541-020-00389-7.
[2] Dupont, R., 2015, Robust Rotor Dynamics for High-speed Air Bearing Spindles. Precision Engineering, 40:7–13. https://doi.org/10.1016/j.precisioneng.2014.12.008.
[3] Guenat, E., Schiffmann, J., 2019, Multi-Objective Optimization of Grooved Gas Journal Bearings for Robustness in Manufacturing Tolerances. Tribology Transactions, 62:1041–1050. https://doi.org/10.1080/10402004.2019.1642547.
[4] Ehrlenspiel, K., Kiewert, A., Lindemann, U., 2007, Cost-efficient Design. Springer Berlin Heidelberg.
[5] Schiffmann, J., Favrat, D., 2010, Integrated Design and Optimization of Gas Bearing Supported Rotors. Journal of Mechanical Design, Transactions of ASME, 132:0510071–05100711. https://doi.org/10.1115/1.4001381.
[6] Cao, Y., Altintas, Y., 2007, Modeling of Spindle-bearing and Machine Tool Systems for Virtual Simulation of Milling Operations. International Journal of Machine Tools and Manufacture, 47:1342–1350. https://doi.org/10.1016/j.ijmachtools.2006.08.006.
[7] Genta, G., 2005, Dynamics of Rotating Systems. Springer US, New York, NY.
[8] Jeffcott, H.H., 1919, XXVII. The Lateral Vibration of Loaded Shafts in the Neighbourhood of a Whirling Speed.— The Effect of Want of Balance. London, Edinburgh, and Dublin Philosophical Magazine and Journal of Science, 37:304–314. https://doi.org/10.1080/14786440308635889.
[9] Steinke, P., 2004, Finite-Elemente-Methode. Springer Berlin Heidelberg.
[10] Poganski, J., Mair, M., Ellermann, K., 2015, A Full Structural Mechanical Description of Beam Elements for Rotors in Electrical Machines. International Journal for Computation and Mathematics in Electrical and Electronic Engineering, 34:1404–1417. https://doi.org/10.1108/COMPEL-02-2015-0058.
[11] Hutchinson, J.R., 2001, Shear Coefficients for Timoshenko Beam Theory. Journal of Applied Mechanics, Transactions ASME, 68:87–92. https://doi.org/10.1115/1.1349417.
[12] Cowper, G.R., 1964, The Shear Coefficient in Timoshenko's Beam Theory. Journal of Applied Mechanics, Transactions ASME, 33:335–340. https://doi.org/10.1115/1.3625046.
[13] Spura, C., 2019, Technische Mechanik 2. Elastostatik. Springer Fachmedien Wiesbaden.
[14] International Organization for Standardization, 2015, ISO 230–7:2015 - Test Code for Machine Tools — Part 7: Geometric Accuracy of Axes of Rotation.
[15] Luo, Y., 2008, An Efficient 3D Timoshenko Beam Element with Consistent Shape Functions. Advances in Theoretical and Applied Mechanics, 1:95–106.
[16] Neto, M.A., Amaro, A., Luis, R., Cirne, J., Leal, R., 2015, Engineering Computation of Structures: The Finite Element Method. Springer International Publishing.
[17] Klein, B., 2015, Fem. Springer Fachmedien Wiesbaden, Wiesbaden.
[18] Vollan, A., Komzsik, L., 2012, Computational Techniques of Rotor Dynamics with the Finite Element Method. CRC Press.
[19] Kumar, D., 2016, MSC Nastran 2016 Rotordynamics User's Guide.
[20] Nelson, H.D., McVaugh, J.M., 1976, The Dynamics of Rotor-bearing Systems Using Finite Elements. Journal of Manufacturing Science and Engineering, Transactions of the ASME, 98:593–600. https://doi.org/10.1115/1.3438942.
[21] Larsonneur R. (2006) Modeling and Analysis of Dynamic Mechanical Systems with a Special Focus on Rotordynamics and Active Magnetic Bearing (AMB) Systems.
[22] Shaw, A.D., Champneys, A.R., Friswell, M.I., 2016, Asynchronous Partial Contact Motion Due to Internal Resonance in Multiple Degree-of-freedom Rotordynamics. in: Proceedings of The Royal Society A Mathematical Physical and Engineering Sciences, 472. https://doi.org/10.1098/rspa.2016.0303.
[23] Pedersen, P.T., 1972, On Forward and Backward Precession of Rotors. Ingenieur-Archiv, 42:26–41. https://doi.org/10.1007/BF00533283.
[24] Chung, J., Hulbert, G.M., 1993, A Time Integration Algorithm for Structural Dynamics with Improved Numerical Dissipation: The Generalized-α Method. Journal of Applied Mechanics, Transactions ASME, 60:371–375. https://doi.org/10.1115/1.2900803.
[25] von Stryk, O., Bulirsch, R., 1992, Direct and Indirect Methods for Trajectory Optimization. Annals of Operations, 37:357–373. https://doi.org/10.1007/BF02071065.

[26] Altintas, Y., Ber, A., 2001, Manufacturing Automation: Metal Cutting Mechanics, Machine Tool Vibrations, and CNC Design. B84–B84 Applied Mechanics Review, 54. https://doi.org/10.1115/1.1399383.
[27] Zio, E., 2013, The Monte Carlo Simulation Method for System Reliability and Risk Analysis. Springer, London.
[28] Altintas, Y., 2012, Manufacturing Automation: Metal Cutting Mechanics, Machine Tooling Vibrations, and CNC Design, 43–46.
[29] Stoop F., Mayr J., Wegener K. (2022) Aerostatic Stiffness and Damping Analysis for High-Speed Air Bearings in Ultra- Precision Machine Tools. in: euspen 22nd International Conference & Exhibition (ICE). Geneva, Switzerland.
[30] Arora, J.S., 2017, Introduction to Optimum Design. Elsevier.
[31] Böhl, S., 2021, Error Identification and Error Correction for Spindle Test Setups. ETH Zurich, Diss. Nr. 27088.
[32] Ostad Ali Akbari, V., Postel, M., Kuffa, M., Wegener, K., 2022, Improving Stability Predictions in Milling by Incorporation of Toolholder Sound Emissions. CIRP Journal of Manufacturing Science and Technology, 37:359–369. https://doi.org/10.1016/J.CIRPJ.2022.02.012.
[33] Kirchgäßner, B., 2016, Finite Elements in Rotordynamics. Procedia Engineering. Elsevier Ltd: 736–750.